CHEMISTRY OF MATERIALS

pubs.acs.org/cm

Article

One-Dimensional Flat Bands and Anisotropic Moiré Excitons in Twisted Tin Sulfide Bilayers

Linghai Zhang, Xu Zhang, and Gang Lu*

Cite This: *Chem. Mater.* 2021, 33, 7432−7440

Read Online

ACCESS | Metrics & More | Article Recommendations | Supporting Information

ABSTRACT: Group IV monochalcogenides have attracted significant recent attention due to their similarities to black phosphorus and their potential applications in "twistronics", inspired by the synthesis of nanowires and nanocrystals with continuous interlayer Eshelby twists. They are also proposed as an ideal platform to study strongly correlated physics with dimensional crossover. However, little is known on moiré superlattices formed by twisted monochalcogenide bilayers. In particular, the optoelectronic properties of the twisted monochalcogenide bilayers are largely unexplored and it is not clear whether moiré excitons can be hosted in such bilayers. In this work, we reveal the structural, optoelectronic, and excitonic properties of twisted SnS bilayers from first-principles. The key aspects of the moiré superlattices, including lattice reconstructions, moiré potentials, formation of flat bands, one-dimensional and anisotropic moiré excitons, and tuning of moiré excitons by twist angle and interlayer distance, are examined.

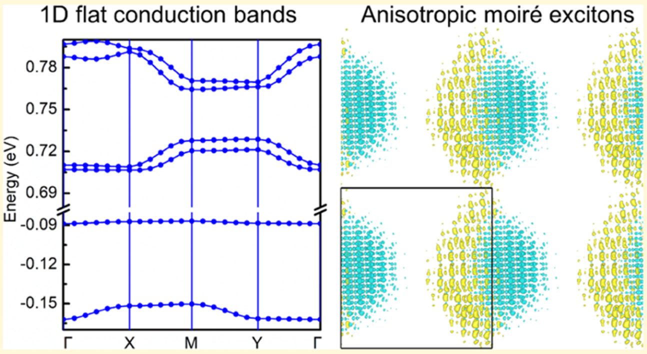

■ INTRODUCTION

When two-dimensional (2D) materials are stacked to form a van der Waals (vdW) heterostructure with a small angular and/or lattice mismatch, a long-range moiré superlattice may appear, which could lead to novel correlated quantum phenomena, driven by the interplay between flat energy bands (i.e., suppressed kinetic energy) and strong electron−electron interactions.[1−6] In particular, the moiré superlattices comprising 2D semiconductors, such as transition-metal dichalcogenides (TMDs), could host localized, long-lived, and valley-polarized moiré excitons,[7−10] which are envisioned as single-photon emitters in quantum information and optoelectronic applications.[11−13] The moiré superlattices have thus emerged as a fascinating and versatile platform to engineer quantum states of matter,[1−6] both for fundamental science and practical applications.

In semiconducting moiré superlattices, TMDs have been the center of interest thanks to their strong light−matter interaction, spin−orbit coupling (SOC), and superior stability. In this work, we focus instead on the group IV monochalcogenides MX (M = Sn or Ge and X = S or Se) and moiré superlattices formed by twisted MX homobilayers. Similar to black phosphorus, few-layer monochalcogenides, such as SnS, are known to possess tunable band gaps, strong in-plane anisotropy, and high electron mobilities.[14] Group IV monochalcogenides are also predicted to exhibit giant piezoelectricity,[15,16] room-temperature ferroelectricity[17,18] and ferroelasticity,[19,20] and a large bulk photovoltaic effect.[21−23]

Our work was inspired by recent breakthroughs in the burgeoning field of "monochalcogenide twistronics". On the experimental side, impressive progress has been made to synthesize GeS vdW nanowires[24] and nanocrystals[25] with a continuous interlayer twist or Eshelby twist; these helical nanostructures can be viewed as continuously twisted GeS homobilayers stacked along the helical axis. The generic fabrication process can be applied to other group IV monochalcogenides (e.g., GeSe).[25] More importantly, the twist angle and the topology in these nanostructures can be tuned synthetically, thus paving the way to twistronic applications of these materials. On the theoretical side, one-dimensional (1D) flat energy bands have been predicted in twisted GeSe bilayers by first-principles calculations.[26] In particular, the twisted GeSe bilayers are proposed as an ideal platform to study strongly correlated 1D physics and the crossover from 1D to 2D physics in a highly tunable manner.[26] Furthermore, it is speculated that by coupling to a superconducting substrate, the twisted GeSe bilayers may host Majorana edge states.

Received: June 22, 2021
Published: September 3, 2021

https://doi.org/10.1021/acs.chemmater.1c02165
Chem. Mater. 2021, 33, 7432−7440

Despite the exciting experimental and theoretical advances, some key aspects pertaining to moiré superlattices of the monochalcogenides remain largely unexplored. Owing to their lower symmetry (C_{2V}), the monochalcogenide vdW bilayers are expected to host anisotropic moiré excitons, in contrast to isotropic moiré excitons observed in TMD bilayers.[7−10] However, there is no report—either from theory or experiment—on the formation of moiré excitons in twisted MX bilayers. The energetic, structural, and optoelectronic properties of monochalcogenide moiré superlattices are yet to be studied. In particular, it is not clear whether 1D moiré excitons can be formed and tuned in twisted monochalcogenide bilayers. Recent experiments reported the formation of 1D moiré excitons in TMD heterobilayers (WSe_2/$MoSe_2$) by applying uniaxial strains.[27] However, since strain distributions are not easily controlled in vdW heterostructures, it would be desirable to generate "intrinsic" 1D moiré excitons in twisted MX bilayers without the application of strains. The anisotropic and 1D moiré excitons could lead to novel applications in quantum information and optoelectronic devices, such as polarization-sensitive photodetectors, polarized light-emitting diodes, and so forth.[28−31]

In this work, we carry out the state-of-the-art first-principles calculations to examine structural, electronic, optical, and excitonic properties of twisted SnS bilayers, with the aim of providing a theoretical foundation for monochalcogenide twistronics. Several twist angles (θ = 3.9, 4.1, 175.9, and 176.1°) are considered for the SnS homobilayer. Key aspects to the moiré superlattices, including lattice reconstructions, moiré potentials, formation of flat bands, 1D and anisotropic moiré excitons, and tuning of moiré excitons by twist angle and interlayer distance, are explored in detail.

METHODS

Density functional theory (DFT) calculations were performed with the Vienna Ab initio Simulation Package (VASP)[32] to examine the ground-state properties of SnS bilayers. The Perdew−Burke−Ernzerhof (PBE)[33] exchange−correlation functional along with the projector-augmented wave pseudopotentials[34] were used in the calculations. An energy cutoff of 400 eV was used in the expansion of the wavefunctions and a Γ-centered 12 × 13 × 1 Monkhorst−Pack k-grid was used to sample the Brillouin zone (BZ) of the nontwisted bilayers. The atomic structures of the twisted SnS bilayers were obtained using CellMatch software.[35] The lattice mismatch in the twisted SnS bilayer for θ = 4.1° (and 175.9°) and θ = 3.9° (and 176.1°) is 0.13 and 0.12%, respectively. Due to the large moiré superlattices (more than 1500 atoms), only the Γ point was sampled in the BZ to obtain the optimized atomic structures and electronic band structures for the twisted bilayers. All atomic structures were optimized until the force acting on each atom was less than 0.01 eV/Å. The Grimme's PBE-D2 correction[36] was used to capture the vdW interaction between SnS layers. A vacuum region of ∼15 Å in the out-of-plane direction was used to eliminate the spurious interaction between the periodical slabs.

To determine the excitonic properties of SnS bilayers, a recently developed first-principles method was used, which is based on linear-response time-dependent DFT (LR-TDDFT)[37,38] with optimally tuned, screened, and range-separated hybrid (OT-SRSH) exchange−correlation functionals.[39−41] In this method, three parameters, α, β, and γ, are required. α controls the short-range exact exchange and β is chosen to satisfy the requirement $\alpha + \beta = 1/\varepsilon_0$; ε_0 is the scalar dielectric constant of the SnS bilayer, set to 7.3 in this work.[42] With the optimal set of the parameters (α = 0.05, β = 0.09, and γ = 0.2) in the DFT-OT-RSH calculations, we obtained the fundamental band gap (1.59 eV) for the nontwisted SnS bilayer, which agrees well with the values (1.57−1.62 eV) reported by others.[14,42] The exciton binding energy E_b, defined as the difference between the fundamental band gap and the optical band gap, is calculated as 0.28 eV for the nontwisted SnS bilayer, which agrees well with the values (0.2−0.3 eV) reported for the group IV monochalcogenides.[43,44] Only the Γ point was sampled in the BZ in these large-scale LR-TDDFT calculations. Our (TD)DFT-OT-RSH method has been successfully applied to various 2D semiconductors and their heterostructures, and more details about the method can be found in our previous works.[45−53] The oscillator strengths were calculated using a newly developed LR-TDDFT method with stochastic and range-separated hybrid functionals.[54] The range-separation parameters used in the stochastic LR-TDDFT calculations were the same as those in the (TD)DFT-OT-RSH calculations.

RESULTS AND DISCUSSION

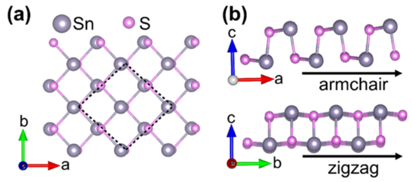

Figure 1. Top view (a) and side view (b) of the SnS monolayer showing the armchair (a-axis) and zigzag (b-axis) directions. The black box (dashed lines) represents a conventional unit cell.

In this work, the stable α phase of the SnS monolayer with a puckered structure, as shown in Figure 1, is used to form homobilayers. In Figure 2a, we display the unit cells of four bilayers (A, B, C, and D) in which the top and bottom layers have a relative shift but without a relative twist (θ = 0°); these are denoted as forward-stacking (FS) structures. One can also switch the cations and anions in the top layers of the four FS structures and arrive at four reverse-stacking (RS) structures (A′, B′, C′, and D′), as shown in Figure 2b, with the corresponding FS and RS structures (e.g., A and A′) related by 180° rotation. These stacking structures appear as local motifs in twisted bilayers as discussed below.

To form a twisted bilayer using the CellMatch software,[35] we stack two SnS monolayers in the FS structure D along the c-axis with a twist angle θ. In Figure 2c,d, we show the non-reconstructed (only the atomic coordinates in the c-axis are optimized) and reconstructed (all coordinates are optimized) structures of a twisted SnS bilayer with a twist angle θ = 4.1°, respectively. Similarly, Figure 2e,f displays the non-reconstructed and reconstructed structures of a twisted SnS bilayer with a twist angle θ = 175.9°, respectively. Note that the moiré superlattices formed by the twisted bilayers with angle θ and 180°−θ have the same lattice constants and the number of atoms. Thus, the moiré superlattices for θ = 4.1° and θ = 175.9° bilayers have the same number of atoms (1564) and the lattice constants (a = 5.63 nm and b = 5.97 nm). These two bilayers exhibit the FS (θ = 4.1°) and RS (θ = 175.9°) structure, respectively.

Similar to other vdW heterostructures, significant lattice reconstruction can develop in twisted SnS bilayers. To visualize the lattice reconstruction, we label the local stacking structures in the superlattices by the motifs A, B, C, and D (or A′, B′, C′, and D′), as shown in Figure 2c−f. The atomic structure of the 4.1° bilayer is dominated by the stacking motifs C and D, while the structure of the 175.9° bilayer is dominated by the stacking motifs C′ and D′ before the reconstruction. After the reconstruction, the areas of domains A (A′) and B (B′)

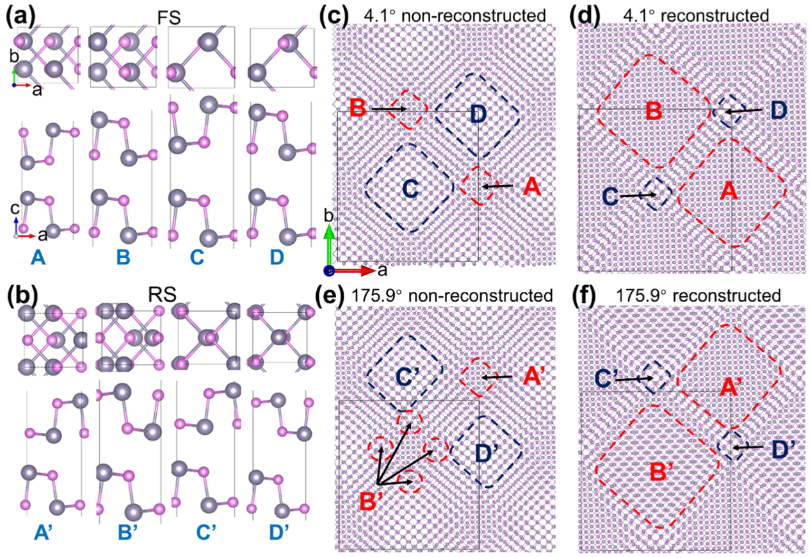

Figure 2. (a) Top and side view of the four FS structures (A, B, C, and D) in a nontwisted SnS bilayer. (b) Top and side view of the four RS structures (A′, B′, C′, and D′) in a nontwisted SnS bilayer. Non-reconstructed (c) and reconstructed (d) twisted bilayer with θ = 4.1° and non-reconstructed (e) and reconstructed (f) twisted bilayer with θ = 175.9°.

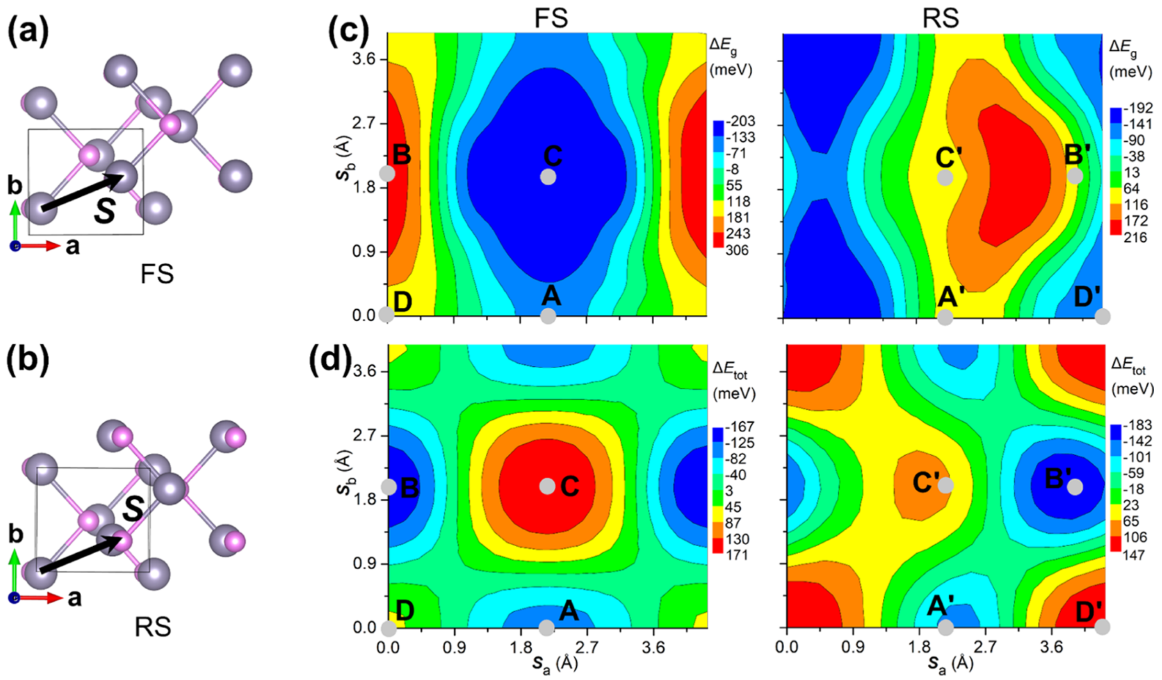

Figure 3. Definition of the interlayer displacement vector (***S***) in the FS (a) and RS (b) structures. (c) Band gap variation (ΔE_g) as a function of the interlayer displacement vector ***S*** (S_a and S_b are the projections of ***S*** in the *a*- and *b*-axis). (d) Total energy variation (ΔE_{tot}) as a function of the interlayer displacement vector ***S***. The approximate locations of the stacking motifs are also indicated. The FS and RS structures are shown in the left and right columns.

grow significantly at the expense of domains C (C′) and D (D′). In addition, the areas of the high-energy domain walls (or solitons) are reduced to lower the energy. The lattice reconstruction is driven primarily by the energetic differences among the four stacking motifs as discussed later. The rectangular domain shape in both bilayers stems from the rectangular unit cell of the SnS monolayer shown in Figure 1a, which is in contrast to triangular domains observed in twisted TMD bilayers (0° < θ < 2°)[55] with hexagonal unit cells. As elucidated below, the lattice reconstruction plays a crucial role in the optoelectronic and excitonic properties of the moiré superlattices.

As the most important feature of a moiré superlattice, the moiré potential determines the band structure, the localization, and the hybridization of moiré excitons. The moiré potential can be defined by the spatial variation of the fundamental gap as a function of the relative in-place displacement between the two monolayers.[11,56,57] In this definition, the moiré potential approximates the exciton energy with the assumption that the exciton binding energy is independent of the in-plane displacement. This is a reasonable approximation since the

Table 1. Band Gap Variation (in meV), the Total Energy Variation (in meV), and the Interlayer Distance (in Å) of the FS and RS Structures

	FS structures				RS structures			
	A	B	C	D	A′	B′	C′	D′
$\Delta E_g(\boldsymbol{S})$	−93	306	−165	159	84	98	95	−141
$\Delta E_{tot}(\boldsymbol{S})$	−94	−167	171	54	−112	−183	74	147
interlayer distance	2.99	2.88	3.64	3.18	2.93	2.86	3.22	3.57

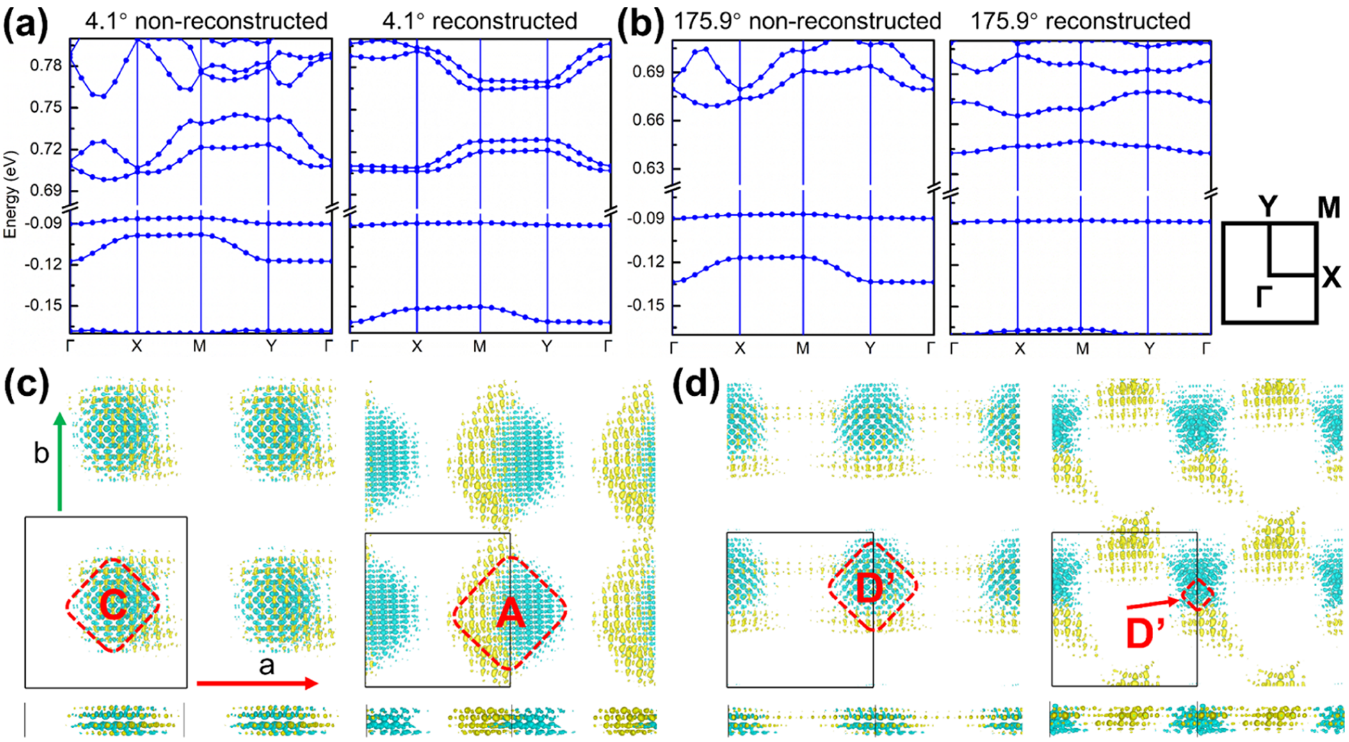

Figure 4. Single-particle band structure of the non-reconstructed and reconstructed 4.1° bilayer (a) and 175.9° bilayer (b). The BZ with high-symmetry *k*-points is also shown. The charge density of the lowest energy moiré exciton in the non-reconstructed and reconstructed 4.1° bilayer (c) and 175.9° bilayer (d). Both the top and side views of the bilayer are shown. The charge density of the hole and the electron is shown in cyan and yellow color, respectively. The moiré supercell is indicated by the black box in (c,d).

exciton binding energy depends primarily on the interlayer distance. As shown in Figure 3a,b, the vector $\boldsymbol{S}$ represents the relative in-plane displacement between two SnS monolayers in the primitive unit cells, and as $\boldsymbol{S}$ spans the entire unit cell, all possible stacking configurations can be obtained. The band gap variation $\Delta E_g(\boldsymbol{S})$ is defined as: $\Delta E_g(\boldsymbol{S}) = E_g(\boldsymbol{S}) - \langle E_g \rangle$, where $E_g(\boldsymbol{S})$ is the band gap of the nontwisted SnS bilayers and $\langle E_g \rangle$ is the average value of E_g. Figure 3c shows the moiré potentials of the SnS bilayer in the FS and RS structures. Compared to TMD bilayers,[52,56,57] the most striking feature of the moiré potentials in SnS bilayers is the strong anisotropy. For either the FS or RS structure, the moiré potential is anisotropic, with its gradient in the *a*-axis much larger than that in the *b*-axis, which is in sharp contrast to the threefold symmetric moiré potentials in TMD bilayers.[52,56,57] The anisotropic moiré potentials in SnS bilayers lead to anisotropic band structures, oscillator strengths, and moiré excitons as discussed below.

The minimum value of the moiré potential in the FS structure is −203 meV, located near the C stacking configuration, whereas the maximum value of the moiré potential is 306 meV, at the B stacking configuration. Thus, the amplitude of the moiré potential in the FS structure is 509 meV. Similarly, the minimum value of the moiré potential in the RS structure is −192 meV, close to the D′ stacking configuration, while the maximum value is 216 meV at the mid point between B′ and C′. The amplitude of the moiré potential in the RS structure is thus 402 meV. As a comparison, the amplitude of the moiré potential in WS_2/MoS_2 heterobilayers is ∼260 meV[52] and the amplitude of the moiré potential in halide perovskite bilayers MA_2PbI_4 is ∼233 meV.[53] Although the moiré superlattices with the twist angles θ and $180°-\theta$ have the same lattice constants, they—in the FS and RS structures—are predicted to have different moiré potentials. Note that the moiré potential determined in this manner represents the upper bound for all SnS bilayers (with the same interlayer distance) because the maximum or minimal energy stacking configurations may not be reachable in a specific twisted bilayer. Finally, the experimental estimate for the moiré potential in the $WSe_2/MoSe_2$ heterobilayer is ∼300 and ∼150 meV for the valence and conduction bands, respectively.[58]

To shed light on the reconstruction of the moiré superlattices, we calculate the energies of the various stacking motifs. In particular, we determine the total energy variation of a nontwisted SnS bilayer, $\Delta E_{tot}(\boldsymbol{S})$, as a function of the displacement $\boldsymbol{S}$, analogous to the moiré potential, that is, $\Delta E_{tot}(\boldsymbol{S}) = E_{tot}(\boldsymbol{S}) - \langle E_{tot} \rangle$. Here, E_{tot} is the total energy of the nontwisted SnS bilayer and $\langle E_{\mathrm{tot}} \rangle$ is the average value of E_{tot}. Hence, $\Delta E_{\mathrm{tot}}(\boldsymbol{S})$ represents the stacking energy landscape in SnS bilayers, and it is called the stacking potential in the following. In Figure 3d, we show the stacking potentials for both FS and RS structures. An interesting anticorrelation is observed between the extremes of the moiré potential and the stacking potential for both structures, that is, the maximum (or minimum) of the moiré potential occurs at the location of the minimum (or maximum) of the stacking potential. Specifically, for the FS structure, the maximum of the stacking potential is located at the C stacking, corresponding to the minimum of the moiré potential; the minimum of the stacking potential resides at the B stacking, corresponding to the maximum of the moiré potential. Similarly, for the RS structure, the maximum of the stacking potential occurs at D′, corresponding to the minimum of the moiré potential. Finally, the minimum of the stacking potential is at B′, which slightly deviates from the maximum of the moiré potential. The amplitude of the stacking potential is 338 and 330 meV for the FS and RS structure, respectively, which is smaller than the amplitude of the moiré potential.

There is also a correlation between the stacking potential and the interlayer distance, as shown in Table 1. For instance, in the FS structure, the shortest interlayer distance occurs at the stacking B (2.88 Å), which has the lowest stacking energy (−167 meV), while the largest interlayer distance is at the stacking C (3.64 Å) with the highest stacking energy (171 meV). The same correlation also holds in the RS structure. Therefore, the interlayer distance plays a crucial role in determining the properties of the moiré superlattices, along with the twist angle. Finally, we note that for both FS and RS structures, the A (A′) and B (B′) stackings have lower energies than the C (C′) and D (D′) stackings; therefore, the reconstruction of the superlattices takes place by growing the lower energy domains of A (A′) and B (B′) at the expense of the higher energy domains of C (C′) and D (D′).

We next determine the single-particle band structures of twisted SnS bilayers with $\theta = 4.1°$ and $\theta = 174.9°$ using the PBE functional. To examine the role of the lattice reconstruction on the band structure, we include in Figure 4a,b the band structures for both non-reconstructed and reconstructed bilayers. The valence band maximum (VBM) has approximately equal contributions from both layers, while the conduction band minimum (CBM) arises primarily from Sn atoms at the top layer (the bottom layer Sn atoms only account for half the contribution of the top layer Sn atoms); the contributions to CBM from S atoms at both layers are negligible. The first important observation from Figure 4 is the formation of a nearly flat VBM (the bandwidth is 2 meV) in both bilayers, independent of the lattice reconstruction. The flat VBM implies localized and strongly correlated holes, which interestingly are not the result of the lattice reconstruction. Instead, the flat VBM stems from the interlayer modulation and the formation of the moiré lattice—the details of the moiré lattice are not important. The second important observation is the formation of 1D flat conduction bands in the reconstructed 4.1° bilayer. More specifically, the CBM and CBM + 1 along the Γ−X and the parallel M−Y direction are nearly flat (the bandwidth is 15 meV); thus, they only disperse along one dimension. The 1D flat conduction bands were also observed in twisted GeSe bilayers.[26] The formation of both the flat VBM and CBM (partially) in twisted SnS bilayers distinguished them from TMD moiré superlattices, where only the VBM is flat. Thus, we predict the co-existence of quasi-1D electrons along the *b*-axis and quasi-0D holes in the twisted 4.1° SnS bilayer. The quasi-1D electron mobility along the *b*-axis remains high with an estimated effective mass of 0.5 m_0.[14] The quasi-1D electron in the *b*-axis is consistent with the fact that the moiré potential gradient is vanishingly small in this direction for the FS structure. Interestingly, the flat conduction bands are not observed in the non-reconstructed 4.1° bilayer. This may be due to the fact that the interlayer Sn−Sn distance in the non-reconstructed bilayer is 0.2 Å larger than the reconstructed bilayer, thus the interlayer modulation is too weak to yield flat conduction bands. Although the VBM remains nearly flat in the 175.9° bilayer, its conduction bands are less flat as compared to the 4.1° bilayer. Thus, the 1D-like electron distribution is not present in the 175.9° bilayer. The difference suggests that the properties of the moiré superlattices are determined by both the twist angle and the stacking structures.

As the inversion symmetry is broken in the twisted SnS bilayers, the Rashba SOC could be important. We thus recalculate the single-particle band structures by including the SOC correction (PBE + SOC). We find that the SOC-induced band splitting is primarily in the conduction bands, while the SOC effect on the valence bands is negligible. As shown in Figure 5, the SOC splitting of CBM in the reconstructed 4.1° bilayer is anisotropic, with a stronger splitting along the Γ−Y direction and a negligible splitting along the Γ−X direction. In contrast, the SOC splitting is less anisotropic in the 175.9° bilayer. For both bilayers, we find that the SOC correction has a minor effect (a few meV) on the bandwidths and the 1D conduction bands remain flat in the 4.1° bilayer. Therefore, to reduce the computational cost, the SOC correction is not included in the following calculations. It is interesting to note that the SOC splitting depends on the stacking structure of nontwisted SnS bilayers. As shown in Figure S1 (in Supporting Information), the SOC splitting is zero in the B′ motif (due to the presence of inversion symmetry) and 80 meV in the A motif; the latter is similar to the SOC splitting (86 meV) in the monolayer SnS.[59] The smaller splitting in twisted bilayers stems from averaged contributions from different local motifs and the formation of moiré superlattices. The latter is expected to reduce the energy difference between SOC-split spin states in the same manner as it does to flatten the bands.

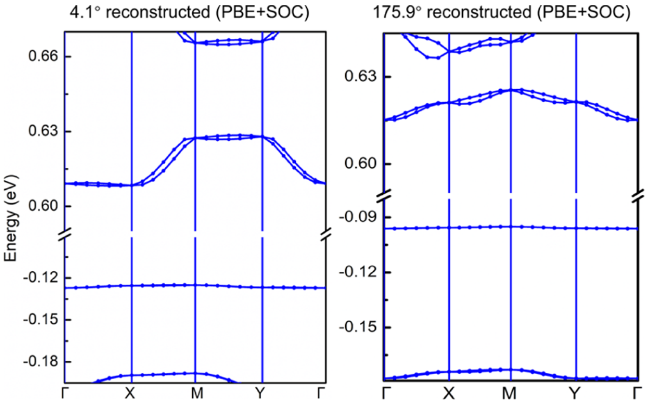

Figure 5. Single-particle band structures of the reconstructed 4.1 and 175.9° SnS bilayer using PBE + SOC calculations.

Next, we examine the properties of moiré excitons. In Figure 4c,d, we present the charge densities of the lowest energy excitons in the twisted SnS bilayers. First of all, consistent with the band structure analysis, the moiré exciton in the reconstructed 4.1° bilayer exhibits a quasi-1D electron and quasi-0D hole distribution. In contrast, the moiré exciton in the non-reconstructed 4.1° bilayer shows 0D distribution for both electrons and holes. Despite the dispersive conduction bands in the non-reconstructed 4.1° bilayer, the electron remains localized and bound by the localized hole, which is a manifestation of the excitonic effect. Second, the lowest moiré exciton resides at the C stacking in the non-reconstructed 4.1° bilayer and at the A stacking in the reconstructed bilayer. Since C has the lowest moiré potential, the exciton is supposed to be trapped at C as opposed to A. However, after the reconstruction, the domain A increases significantly at the expense of the domain C (see Figure 2d). As the moiré potential at A is only slightly higher than C, the exciton can actually be stabilized at A in the reconstructed bilayer. In contrast to the 4.1° bilayer, the lowest moiré exciton in the 175.9° bilayer does not exhibit a 1D-like electron distribution, regardless of the lattice reconstruction. Instead, both the electron and hole are localized at D′ owing to its lower moiré potential, particularly for the non-reconstructed bilayer. The reconstruction leads to a partial separation of the electron and the hole, driven by the delocalized electron states (i.e., the dispersive conduction bands). Third, the moiré excitons in both bilayers exhibit hybrid interlayer−intralayer characteristics owing to negligible band offsets in the twisted homobilayers. Finally, we have also examined a few moiré excitons with slightly higher energies and their charge densities are similar to that of the lowest moiré exciton (Figure S2), suggesting that the same flat valence and conduction bands are involved in these excitons.

To examine the optical properties of the twisted SnS bilayers, we calculate the oscillator strength of the lowest energy exciton before and after the lattice reconstruction. As shown in Figure 6, for both bilayers, the oscillator strength of the lowest exciton increases by more than one order of magnitude after the lattice reconstruction. We have previously shown that the transition dipole moment is proportional to the overlap between the electron and hole wavefunctions (but not the charge densities) and inversely proportional to the square root of the excitation energy.[60] The oscillator strength is proportional to the square of the transition dipole moment. Since the excitons here have similar energies, we believe that the dominant contribution to the larger oscillator strengths in the reconstructed lattices is due to their greater overlap between the electron and hole wavefunctions. The overlap cancellation between the oppositely signed electron and hole wavefunctions yields much smaller oscillator strengths in the non-reconstructed bilayers. The oscillator strengths in the reconstructed lattices exhibit significant anisotropy, particularly for 175.9° which has a much higher oscillator strength along the *b*-axis than the other two directions. Similar anisotropy is also observed in higher-energy moiré excitons. The anisotropy in the oscillator strength is consistent with a previous report on the anisotropy of optical absorption in the SnS bilayer where the low-energy absorption along the *b*-axis is stronger than the other directions.[42]

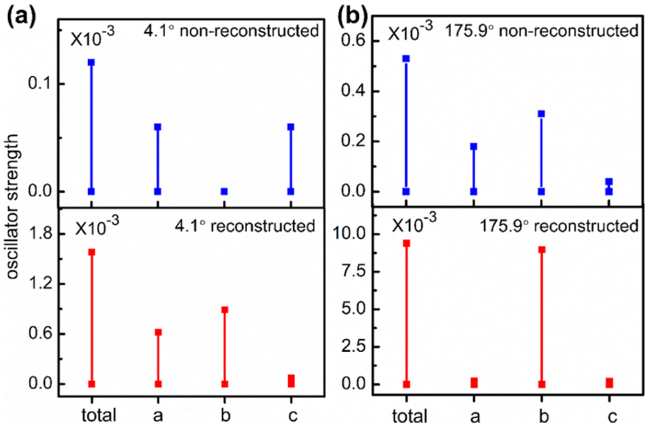

Figure 6. (a) Oscillator strength of the lowest exciton in the non-reconstructed and reconstructed 4.1° bilayer (a) and 175.9° bilayer (b). Both the total and a-, b-, and c-components are shown.

As alluded to earlier, the twist angle and the interlayer distance are two key parameters that can affect the properties of moiré superlattices. In the following, we examine how moiré excitons can be tuned by the twist angle and the interlayer distance. To this end, two additional twisted angles (θ = 3.9 and 176.1°) are considered which yield the same lattice constants (a = 6.06 nm and b = 6.37 nm) and the same number of atoms (1796) in the moiré superlattices. The fully relaxed atomic structure and the charge density of the lowest exciton are presented in Figure 7a,b for both bilayers; their corresponding band structures can be found in Figure S3. While the exciton charge density remains essentially the same between 4.1 and 3.9°, significant changes take place as the angle increases from 175.9 to 176.1°. The exciton charge density becomes more localized in 176.1°, particularly for the electron whose distribution at C′ disappears. For both bilayers, the electron and the hole are partially separated—along the *a*-axis for 3.9° and along the *b*-axis for 176.1°, yielding dipole moments in both directions. The presence of both in-plane and out-of-plane dipole moments suggests that the moiré excitons can be tuned by the respective electric fields, rendering them highly electric field addressable.

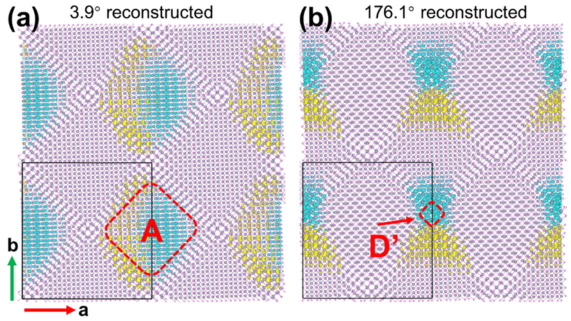

Figure 7. Charge density of the lowest energy exciton in the reconstructed 3.9 (a) and 176.1° (b) SnS bilayer. The charge density of the hole and the electron is shown in cyan and yellow color, respectively. The moiré supercell is indicated by the black box.

We have also reduced the interlayer distance for both bilayers (θ = 4.1 and 175.9°) by 0.2 and 0.4 Å from their equilibrium distances and the exciton charge densities are shown in Figure S4. Similar to what is observed above, there is a negligible change to the exciton charge density in the 4.1° bilayer as the interlayer distance is decreased. However, the exciton charge density alters considerably in the 175.9° bilayer. Once again, the electron distribution at C′ disappears when the interlayer distance is reduced by 0.4 Å. Thus, although the moiré excitons in SnS bilayers can be tuned by both twist angle and interlayer distance, some bilayers are more tunable than others. With a less-symmetric atomic structure (see Figure 3d), the 175.9° bilayer with the RS structure appears more amenable to external tuning. On the other hand, the excitons in the 4.1° bilayer with the FS structure seem more robust. This difference may result from the fact that the FS structures tend to have higher moiré potentials than the RS structures.

■ CONCLUSIONS

To summarize, we have examined the moiré superlattices and moiré excitons in twisted SnS bilayers by means of first-principles calculations, including two FS structures with the twist angle θ = 3.9 and 4.1° and two RS structures with the twist angle θ = 175.9 and 176.1°. Significant lattice reconstruction is observed, driven by the energetic differences among the four stacking motifs. The moiré potentials of the superlattices in both FS and RS structures are shown to exhibit strong anisotropy, yielding anisotropic band structures, oscillator strengths, and moiré excitons. An anticorrelation is observed between the extremes of the moiré potential and the stacking potential, and the stacking potential is further correlated with the interlayer distance. A nearly flat valence band is formed in conjunction with the formation of 1D flat conduction bands in the reconstructed 4.1° bilayer, which leads to strongly correlated quasi-1D electrons and quasi-0D holes in the twisted SnS bilayer. Anisotropic band splitting is found in the conduction bands due to the Rashba effect, which has negligible influence on the valence bands. The twisted bilayers host localized and anisotropic moiré excitons which exhibit hybrid interlayer−intralayer characteristics and anisotropic oscillator strengths. We find that both the twist angle and the interlayer distance can be used to tune the moiré excitons, and the excitons in the RS structures are more tunable than those in the FS structures. Our work provides a theoretical foundation to realize anisotropic optoelectronic and quantum computing applications in twisted monochalcogenide nanostructures.

■ ASSOCIATED CONTENT

Supporting Information

The Supporting Information is available free of charge at https://pubs.acs.org/doi/10.1021/acs.chemmater.1c02165.

> Conduction band splitting in nontwisted bilayers; charge densities of higher-energy moiré excitons; band structures of the reconstructed 3.9 and 176.1° bilayers; and exciton charge densities in twisted bilayers with different interlayer distances (PDF)

■ AUTHOR INFORMATION

Corresponding Author

Gang Lu − *Department of Physics and Astronomy, California State University, Northridge, California 91330-8268, United States;* orcid.org/0000-0002-9168-8968; Email: ganglu@csun.edu

Authors

Linghai Zhang − *Department of Physics and Astronomy, California State University, Northridge, California 91330-8268, United States;* orcid.org/0000-0003-0536-5765

Xu Zhang − *Department of Physics and Astronomy, California State University, Northridge, California 91330-8268, United States;* orcid.org/0000-0002-6491-3234

Complete contact information is available at: https://pubs.acs.org/10.1021/acs.chemmater.1c02165

Notes

The authors declare no competing financial interest.

■ ACKNOWLEDGMENTS

This work was supported by the US National Science Foundation (DMR1828019) and the US Army Research Office (W911NF-20-10305).

■ REFERENCES

(1) Cao, Y.; Fatemi, V.; Demir, A.; Fang, S.; Tomarken, S. L.; Luo, J. Y.; Sanchez-Yamagishi, J. D.; Watanabe, K.; Taniguchi, T.; Kaxiras, E.; Ashoori, R. C.; Jarillo-Herrero, P. Correlated Insulator Behaviour at Half-Filling in Magic-Angle Graphene Superlattices. *Nature* **2018**, *556*, 80−84.

(2) Cao, Y.; Fatemi, V.; Fang, S.; Watanabe, K.; Taniguchi, T.; Kaxiras, E.; Jarillo-Herrero, P. Unconventional Superconductivity in Magic-Angle Graphene Superlattices. *Nature* **2018**, *556*, 43−50.

(3) Regan, E. C.; Wang, D.; Jin, C.; Bakti Utama, M. I.; Gao, B.; Wei, X.; Zhao, S.; Zhao, W.; Zhang, Z.; Yumigeta, K.; Blei, M.; Carlström, J. D.; Watanabe, K.; Taniguchi, T.; Tongay, S.; Crommie, M.; Zettl, A.; Wang, F. Mott and Generalized Wigner Crystal States in WSe_2/WS_2 Moiré Superlattices. *Nature* **2020**, *579*, 359−363.

(4) Tang, Y.; Li, L.; Li, T.; Xu, Y.; Liu, S.; Barmak, K.; Watanabe, K.; Taniguchi, T.; MacDonald, A. H.; Shan, J.; Mak, K. F. Simulation of Hubbard Model Physics in WSe_2/WS_2 Moiré Superlattices. *Nature* **2020**, *579*, 353−358.

(5) Wang, Z.; Rhodes, D. A.; Watanabe, K.; Taniguchi, T.; Hone, J. C.; Shan, J.; Mak, K. F. Evidence of High-Temperature Exciton Condensation in Two-Dimensional Atomic Double Layers. *Nature* **2019**, *574*, 76−80.

(6) Dean, C. R.; Wang, L.; Maher, P.; Forsythe, C.; Ghahari, F.; Gao, Y.; Katoch, J.; Ishigami, M.; Moon, P.; Koshino, M.; Taniguchi, T.; Watanabe, K.; Shepard, K. L.; Hone, J.; Kim, P. Hofstadter's Butterfly and the Fractal Quantum Hall Effect in Moiré Superlattices. *Nature* **2013**, *497*, 598−602.

(7) Seyler, K. L.; Rivera, P.; Yu, H.; Wilson, N. P.; Ray, E. L.; Mandrus, D. G.; Yan, J.; Yao, W.; Xu, X. Signatures of Moiré-Trapped Valley Excitons in $MoSe_2/WSe_2$ Heterobilayers. *Nature* **2019**, *567*, 66−70.

(8) Tran, K.; Moody, G.; Wu, F.; Lu, X.; Choi, J.; Kim, K.; Rai, A.; Sanchez, D. A.; Quan, J.; Singh, A.; Embley, J.; Zepeda, A.; Campbell, M.; Autry, T.; Taniguchi, T.; Watanabe, K.; Lu, N.; Banerjee, S. K.; Silverman, K. L.; Kim, S.; Tutuc, E.; Yang, L.; MacDonald, A. H.; Li, X. Evidence for Moiré Excitons in van der Waals Heterostructures. *Nature* **2019**, *567*, 71−75.

(9) Alexeev, E. M.; Ruiz-Tijerina, D. A.; Danovich, M.; Hamer, M. J.; Terry, D. J.; Nayak, P. K.; Ahn, S.; Pak, S.; Lee, J.; Sohn, J. I.; Molas, M. R.; Koperski, M.; Watanabe, K.; Taniguchi, T.; Novoselov, K. S.; Gorbachev, R. V.; Shin, H. S.; Fal'ko, V. I.; Tartakovskii, A. I. Resonantly Hybridized Excitons in Moiré Superlattices in van der Waals Heterostructures. *Nature* **2019**, *567*, 81−86.

(10) Jin, C.; Regan, E. C.; Yan, A.; Iqbal Bakti Utama, M.; Wang, D.; Zhao, S.; Qin, Y.; Yang, S.; Zheng, Z.; Shi, S.; Watanabe, K.; Taniguchi, T.; Tongay, S.; Zettl, A.; Wang, F. Observation of Moiré Excitons in WSe_2/WS_2 Heterostructure Superlattices. *Nature* **2019**, *567*, 76−80.

(11) Yu, H.; Liu, G.-B.; Tang, J.; Xu, X.; Yao, W. Moiré Excitons: From Programmable Quantum Emitter Arrays to Spin-Orbit−Coupled Artificial Lattices. *Sci. Adv.* **2017**, *3*, No. e1701696.

(12) Baek, H.; Brotons-Gisbert, M.; Koong, Z. X.; Campbell, A.; Rambach, M.; Watanabe, K.; Taniguchi, T.; Gerardot, B. D. Highly

Energy-Tunable Quantum Light from Moiré-Trapped Excitons. *Sci. Adv.* **2020**, *6*, No. eaba8526.

(13) Unuchek, D.; Ciarrocchi, A.; Avsar, A.; Watanabe, K.; Taniguchi, T.; Kis, A. Room-Temperature Electrical Control of Exciton Flux in a van der Waals Heterostructure. *Nature* **2018**, *560*, 340−344.

(14) Xin, C.; Zheng, J.; Su, Y.; Li, S.; Zhang, B.; Feng, Y.; Pan, F. Few-Layer Tin Sulfide: A New Black-Phosphorus-Analogue 2D Material with a Sizeable Band Gap, Odd−Even Quantum Confinement Effect, and High Carrier Mobility. *J. Phys. Chem. C* **2016**, *120*, 22663−22669.

(15) Fei, R.; Li, W.; Li, J.; Yang, L. Giant Piezoelectricity of Monolayer Group IV Monochalcogenides: SnSe, SnS, GeSe, and GeS. *Appl. Phys. Lett.* **2015**, *107*, 173104.

(16) Gomes, L. C.; Carvalho, A.; Castro Neto, A. H. Enhanced Piezoelectricity and Modified Dielectric Screening of Two-Dimensional Group-IV Monochalcogenides. *Phys. Rev. B: Condens. Matter Mater. Phys.* **2015**, *92*, 214103.

(17) Mehboudi, M.; Fregoso, B. M.; Yang, Y.; Zhu, W.; van der Zande, A.; Ferrer, J.; Bellaiche, L.; Kumar, P.; Barraza-Lopez, S. Structural Phase Transition and Material Properties of Few-Layer Monochalcogenides. *Phys. Rev. Lett.* **2016**, *117*, 246802.

(18) Fei, R.; Kang, W.; Yang, L. Ferroelectricity and Phase Transitions in Monolayer Group-IV Monochalcogenides. *Phys. Rev. Lett.* **2016**, *117*, 097601.

(19) Wang, H.; Qian, X. Two-Dimensional Multiferroics in Monolayer Group IV Monochalcogenides. *2D Mater* **2017**, *4*, 015042.

(20) Wu, M.; Zeng, X. C. Intrinsic Ferroelasticity and/or Multiferroicity in Two-Dimensional Phosphorene and Phosphorene Analogues. *Nano Lett.* **2016**, *16*, 3236−3241.

(21) Rangel, T.; Fregoso, B. M.; Mendoza, B. S.; Morimoto, T.; Moore, J. E.; Neaton, J. B. Large Bulk Photovoltaic Effect and Spontaneous Polarization of Single-Layer Monochalcogenides. *Phys. Rev. Lett.* **2017**, *119*, 067402.

(22) Murgatroyd, P. A. E.; Smiles, M. J.; Savory, C. N.; Shalvey, T. P.; Swallow, J. E. N.; Fleck, N.; Robertson, C. M.; Jäckel, F.; Alaria, J.; Major, J. D.; Scanlon, D. O.; Veal, T. D. GeSe: Optical Spectroscopy and Theoretical Study of a van der Waals Solar Absorber. *Chem. Mater.* **2020**, *32*, 3245−3253.

(23) Yang, W.; Zhang, X.; Tilley, S. D. Emerging Binary Chalcogenide Light Absorbers: Material Specific Promises and Challenges. *Chem. Mater.* **2021**, *33*, 3467−3489.

(24) Sutter, P.; Wimer, S.; Sutter, E. Chiral Twisted van der Waals Nanowires. *Nature* **2019**, *570*, 354−357.

(25) Liu, Y.; Wang, J.; Kim, S.; Sun, H.; Yang, F.; Fang, Z.; Tamura, N.; Zhang, R.; Song, X.; Wen, J.; Xu, B. Z.; Wang, M.; Lin, S.; Yu, Q.; Tom, K. B.; Deng, Y.; Turner, J.; Chan, E.; Jin, D.; Ritchie, R. O.; Minor, A. M.; Chrzan, D. C.; Scott, M. C.; Yao, J. Helical van der Waals Crystals with Discretized Eshelby Twist. *Nature* **2019**, *570*, 358−362.

(26) Kennes, D. M.; Xian, L.; Claassen, M.; Rubio, A. One-Dimensional Flat Bands in Twisted Bilayer Germanium Selenide. *Nat. Commun.* **2020**, *11*, 1124.

(27) Bai, Y.; Zhou, L.; Wang, J.; Wu, W.; McGilly, L. J.; Halbertal, D.; Lo, C. F. B.; Liu, F.; Ardelean, J.; Rivera, P.; Finney, N. R.; Yang, X.-C.; Basov, D. N.; Yao, W.; Xu, X.; Hone, J.; Pasupathy, A. N.; Zhu, X.-Y. Excitons in Strain-Induced One-Dimensional Moiré Potentials at Transition Metal Dichalcogenide Heterojunctions. *Nat. Mater.* **2020**, *19*, 1068−1073.

(28) Tan, D.; Zhang, W.; Wang, X.; Koirala, S.; Miyauchi, Y.; Matsuda, K. Polarization-Sensitive and Broadband Germanium Sulfide Photodetectors with Excellent High-Temperature Performance. *Nanoscale* **2017**, *9*, 12425−12431.

(29) Wang, X.; Jones, A. M.; Seyler, K. L.; Tran, V.; Jia, Y.; Zhao, H.; Wang, H.; Yang, L.; Xu, X.; Xia, F. Highly Anisotropic and Robust Excitons in Monolayer Black Phosphorus. *Nat. Nanotechnol.* **2015**, *10*, 517−521.

(30) Yang, H.; Jussila, H.; Autere, A.; Komsa, H.-P.; Ye, G.; Chen, X.; Hasan, T.; Sun, Z. Optical Waveplates Based on Birefringence of Anisotropic Two-Dimensional Layered Materials. *ACS Photonics* **2017**, *4*, 3023−3030.

(31) Wang, J.; Zhou, Y. J.; Xiang, D.; Ng, S. J.; Watanabe, K.; Taniguchi, T.; Eda, G. Polarized Light-Emitting Diodes Based on Anisotropic Excitons in Few-Layer ReS_2. *Adv. Mater.* **2020**, *32*, 2001890.

(32) Kresse, G.; Furthmüller, J. Efficient Iterative Schemes for Ab Initio Total-Energy Calculations Using a Plane-Wave Basis Set. *Phys. Rev. B: Condens. Matter Mater. Phys.* **1996**, *54*, 11169−11186.

(33) Perdew, J. P.; Burke, K.; Ernzerhof, M. Generalized Gradient Approximation Made Simple. *Phys. Rev. Lett.* **1996**, *77*, 3865−3868.

(34) Blöchl, P. E. Projector Augmented-Wave Method. *Phys. Rev. B: Condens. Matter Mater. Phys.* **1994**, *50*, 17953−17979.

(35) Lazić, P. Cellmatch: Combining Two Unit Cells into a Common Supercell with Minimal Strain. *Comput. Phys. Commun.* **2015**, *197*, 324−334.

(36) Grimme, S. Semiempirical GGA-Type Density Functional Constructed with a Long-Range Dispersion Correction. *J. Comput. Chem.* **2006**, *27*, 1787−1799.

(37) Runge, E.; Gross, E. K. U. Density-Functional Theory for Time-Dependent Systems. *Phys. Rev. Lett.* **1984**, *52*, 997−1000.

(38) Gross, E. K. U.; Kohn, W. Local Density-Functional Theory of Frequency-Dependent Linear Response. *Phys. Rev. Lett.* **1985**, *55*, 2850−2852.

(39) Refaely-Abramson, S.; Sharifzadeh, S.; Govind, N.; Autschbach, J.; Neaton, J. B.; Baer, R.; Kronik, L. Quasiparticle Spectra from a Nonempirical Ptimally Tuned Range-Separated Hybrid Density Functional. *Phys. Rev. Lett.* **2012**, *109*, 226405.

(40) Refaely-Abramson, S.; Jain, M.; Sharifzadeh, S.; Neaton, J. B.; Kronik, L. Solid-State Optical Absorption from Optimally Tuned Time-Dependent Range-Separated Hybrid Density Functional Theory. *Phys. Rev. B: Condens. Matter Mater. Phys.* **2015**, *92*, 081204.

(41) Kronik, L.; Neaton, J. B. Excited-State Properties of Molecular Solids from First Principles. *Annu. Rev. Phys. Chem.* **2016**, *67*, 587−616.

(42) Tritsaris, G. A.; Malone, B. D.; Kaxiras, E. Optoelectronic Properties of Single-Layer, Double-Layer, and Bulk Tin Sulfide: A Theoretical Study. *J. Appl. Phys.* **2013**, *113*, 233507.

(43) Shi, G.; Kioupakis, E. Anisotropic Spin Transport and Strong Visible-Light Absorbance in Few-Layer SnSe and GeSe. *Nano Lett.* **2015**, *15*, 6926−6931.

(44) Yang, J.-H.; Gong, X.-G. Stacking Induced Indirect-to-Direct Bandgap Transition in Layered Group-IV Monochalcogenides for Ideal Optoelectronics. *J. Mater. Chem. C* **2019**, *7*, 11858−11867.

(45) Huang, L.-y.; Zhang, X.; Zhang, M.; Lu, G. Effect of Point Defects on Optical Properties of Graphene Fluoride: A First-Principles Study. *J. Phys. Chem. C* **2017**, *121*, 12855−12862.

(46) Huang, L.-y.; Zhang, X.; Zhang, M.; Lu, G. Optically Inactive Defects in Monolayer and Bilayer Phosphorene: A First-Principles Study. *Phys. Rev. Mater.* **2018**, *2*, 054003.

(47) Liu, J.; Zhang, X.; Lu, G. Excitonic Effect Drives Ultrafast Dynamics in van der Waals Heterostructures. *Nano Lett.* **2020**, *20*, 4631−4637.

(48) Zhang, L.; Zhang, X.; Lu, G. Intramolecular Band Alignment and Spin−Orbit Coupling in Two-Dimensional Halide Perovskites. *J. Phys. Chem. Lett.* **2020**, *11*, 6982−6989.

(49) Liu, J.; Li, Z.; Wang, J.; Zhang, X.; Zhan, X.; Lu, G. Charge Separation Boosts Exciton Diffusion in Fused Ring Electron Acceptors. *J. Mater. Chem. A* **2020**, *8*, 23304−23312.

(50) Zhang, L.; Zhang, X.; Lu, G. Band Alignment in Two-Dimensional Halide Perovskite Heterostructures: Type I or Type II? *J. Phys. Chem. Lett.* **2020**, *11*, 2910−2916.

(51) Gao, Y.; Zhang, M.; Zhang, X.; Lu, G. Decreasing Exciton Binding Energy in Two-Dimensional Halide Perovskites by Lead Vacancies. *J. Phys. Chem. Lett.* **2019**, *10*, 3820−3827.

(52) Guo, H.; Zhang, X.; Lu, G. Shedding Light on Moiré Excitons: A First-Principles Perspective. *Sci. Adv.* **2020**, *6*, No. eabc5638.

(53) Zhang, L.; Zhang, X.; Lu, G. Predictions of Moiré Excitons in Twisted Two-Dimensional Organic−Inorganic Halide Perovskites. *Chem. Sci.* **2021**, *12*, 6073−6080.

(54) Zhang, X.; Lu, G.; Baer, R.; Rabani, E.; Neuhauser, D. Linear-Response Time-Dependent Density Functional Theory with Stochastic Range-Separated Hybrids. *J. Chem. Theory Comput.* **2020**, *16*, 1064−1072.

(55) Quan, J.; Linhart, L.; Lin, M.-L.; Lee, D.; Zhu, J.; Wang, C.-Y.; Hsu, W.-T.; Choi, J.; Embley, J.; Young, C.; Taniguchi, T.; Watanabe, K.; Shih, C.-K.; Lai, K.; MacDonald, A. H.; Tan, P.-H.; Libisch, F.; Li, X. Phonon Renormalization in Reconstructed MoS_2 Moiré Superlattices. *Nat. Mater.* **2021**, *20*, 1100−1105.

(56) Wu, F.; Lovorn, T.; MacDonald, A. H. Topological Exciton Bands in Moiré Heterojunctions. *Phys. Rev. Lett.* **2017**, *118*, 147401.

(57) Wu, F.; Lovorn, T.; MacDonald, A. H. Theory of Optical Absorption by Interlayer Excitons in Transition Metal Dichalcogenide Heterobilayers. *Phys. Rev. B: Condens. Matter Mater. Phys.* **2018**, *97*, 035306.

(58) Shabani, S.; Halbertal, D.; Wu, W.; Chen, M.; Liu, S.; Hone, J.; Yao, W.; Basov, D. N.; Zhu, X.; Pasupathy, A. N. Deep Moiré Potentials in Twisted Transition Metal Dichalcogenide Bilayers. *Nat. Phys.* **2021**, *17*, 720−725.

(59) Gomes, L. C.; Carvalho, A. Phosphorene Analogues: Isoelectronic Two-Dimensional Group-IV Monochalcogenides with Orthorhombic Structure. *Phys. Rev. B: Condens. Matter Mater. Phys.* **2015**, *92*, 085406.

(60) Zhang, X.; Li, Z.; Lu, G. First-Principles Simulations of Exciton Diffusion in Organic Semiconductors. *Phys. Rev. B: Condens. Matter Mater. Phys.* **2011**, *84*, 235208.